DOI: 10.1089/genbio.2023.0035





# **RESEARCH ARTICLE: SPATIAL OMICS**

# From Ultraviolet to Near-Infrared: Label-Free Reflection-Mode Hyperspectral Photoacoustic Microscopy for Single-Cell Biochemical Mapping

Qiangzhou Rong,<sup>1,†,\*</sup> Carlos Taboada,<sup>1,†</sup> Ángela del Águila,<sup>2</sup> Ilaria Merutka,<sup>3</sup> Nishad Jayasundara,<sup>3</sup> Yushun Zeng,<sup>4</sup> Wei Yang,<sup>2</sup> Qifa Zhou,<sup>4</sup> and Junjie Yao<sup>1,\*</sup>

#### **Abstract**

Hyperspectral imaging has emerged as a valuable technique for analyzing biological tissue compositions by probing intrinsic or exogenous biomolecules. However, conventional hyperspectral imaging methods predominantly rely on fluorescent signatures, limiting their application to nonfluorescent samples. To overcome this limitation, a label-free reflection-mode hyperspectral photoacoustic microscopy (RHS-PAM) system has been developed. RHS-PAM enables the imaging of thick biological samples with a wide range of intrinsic contrasts using excitation wavelengths ranging from ultraviolet to near infrared. RHS-PAM eliminates the need for tissue staining, and has achieved cellular-level spatial resolution and automatic image coregistrations at all wavelengths. Proof-of-concept applications of RHS-PAM have been demonstrated on various model organisms, including Caenorhabditis elegans, frog tadpole, zebrafish, and mouse. The technique has successfully imaged a wealth of structural and molecular features in these organisms, utilizing the optical absorption contrast of nucleic acids, proteins, hemoglobin, melanin, and lipids. The results highlight the capability of RHS-PAM to provide rich optical contrast, high spatial resolution, and an extended spectral range for label-free imaging. We believe that RHS-PAM represents a highly promising tool for single-cell biochemical mapping of diverse biological tissues.

any biological tissues exhibit unique optical signatures or "fingerprints," due to the light-matter interactions such as optical absorption, scattering, reflection, and polarization. Hyperspectral imaging exploits these signatures to map the distribution of biomolecules in tissues, and offers a wealth of functional and molecular information.<sup>1–4</sup> For example, protein and lipid distributions have been used in hyperspectrum imaging to delineate brain tumor margins, providing histologylike images similar to hematoxylin and eosin staining.<sup>5,6</sup> However, traditional hyperspectral imaging methods predominantly rely on fluorescent emission of the targets, <sup>7,8</sup> and thus cannot characterize nonfluorescent samples, which has limited its applications in biomedical research.

Photoacoustic microscopy (PAM) is a hybrid imaging tool that acoustically detects optical contrast based on the photoacoustic effect—the generation of sound waves by the sample's lightabsorbing chromophores, fluorescent or not.9-11 PAM techniques have been developed for histology-like imaging to probe tissue compositions. 12-18 Each tissue composition may provide a unique photoacoustic spectrum when measured at different excitation wavelengths.

For example, nucleic acids (DNA/RNA) are imaged by PAM using ultraviolet (UV) light ~266 nm, which can help identify tumor cells with characteristic nucleus morphological features. 19,20 Hemoglobin is imaged mostly using visible light, which can be used to monitor cancer angiogenesis and hypoxia. 21,22 Lipids are one of the major optical absorbers in the near infrared (NIR) and mid-infrared wavelength range, and can be used to detect lipid-rich diseases such as atherosclerosis. 23,24

Similar to conventional hyperspectrum imaging, multispectral PAM techniques have been developed to identify endogenous biological contrasts in tissues, by using tunable or supercontinuum lasers.<sup>25–27</sup> However, current multispectral PAM techniques, either in reflection mode or transmission mode, have

Departments of <sup>1</sup>Biomedical Engineering and <sup>2</sup>Anesthesiology, Duke University, Durham, North Carolina, USA; <sup>3</sup>The Nicholas School of the Environment, Duke University, Durham, North Carolina, USA; and <sup>4</sup>Department of Biomedical Engineering, University of Southern California, Los Angeles, California, USA. These authors contributed equally to this study.

<sup>\*</sup>Address correspondence to: Qiangzhou Rong, Department of Biomedical Engineering, Duke University, Durham, NC 27708, USA, E-mail: qiangzhou.rong@duke.edu; Junjie Yao, Department of Biomedical Engineering, Duke University, Durham, NC 27708, USA, E-mail: junjie.yao@duke.edu

major limitations. The reflection-mode PAM systems have to use complex optical–acoustic combiners that introduce chromatic aberration and limit the wavelength tuning in the UV and NIR range.<sup>28–30</sup> The transmission-mode PAM systems, in contrast, have limited working space, making these techniques applicable only to thin samples.<sup>23–25</sup> For these reasons, multispectral PAM techniques have been mostly used for imaging of *ex vivo* tissue samples with a limited spectral range.

Here we have developed a new reflection-mode hyperspectrum PAM technique reflection-mode hyperspectral PAM (RHS-PAM) for label-free imaging of multiple biomolecular contrasts on thick *ex vivo* biological tissues and *in vivo* animal models. The wide wavelength tuning range of the excitation light provides access to different endogenous contrasts, including DAN/RNA and proteins using deep UV light, hemoglobin and melanin using visible light, and lipids using NIR light. We demonstrated the flexible application of the RHS-PAM system by investigating the rich morphological, functional, or molecular features of several common animal models—roundworm *Caenorhabditis elegans*, frog tadpoles, zebrafish, and mice.

#### **Results**

#### **RHS-PAM** system

The RHS-PAM system is depicted in Figure 1a. The laser path is divided into four spectral bands ranging from UV to NIR, and is

combined and coupled into a broadband reflective objective lens (ROL). Different excitation wavelength bands are used for imaging various contrasts (Fig. 1b). Samples are placed beneath the ROL with a thin layer of water ( $\sim\!1$  mm) as the coupling medium for acoustic waves. The resultant photoacoustic signals are detected by a high-frequency miniaturized needle transducer (NT). NT is 0.5 mm from the sample surface.

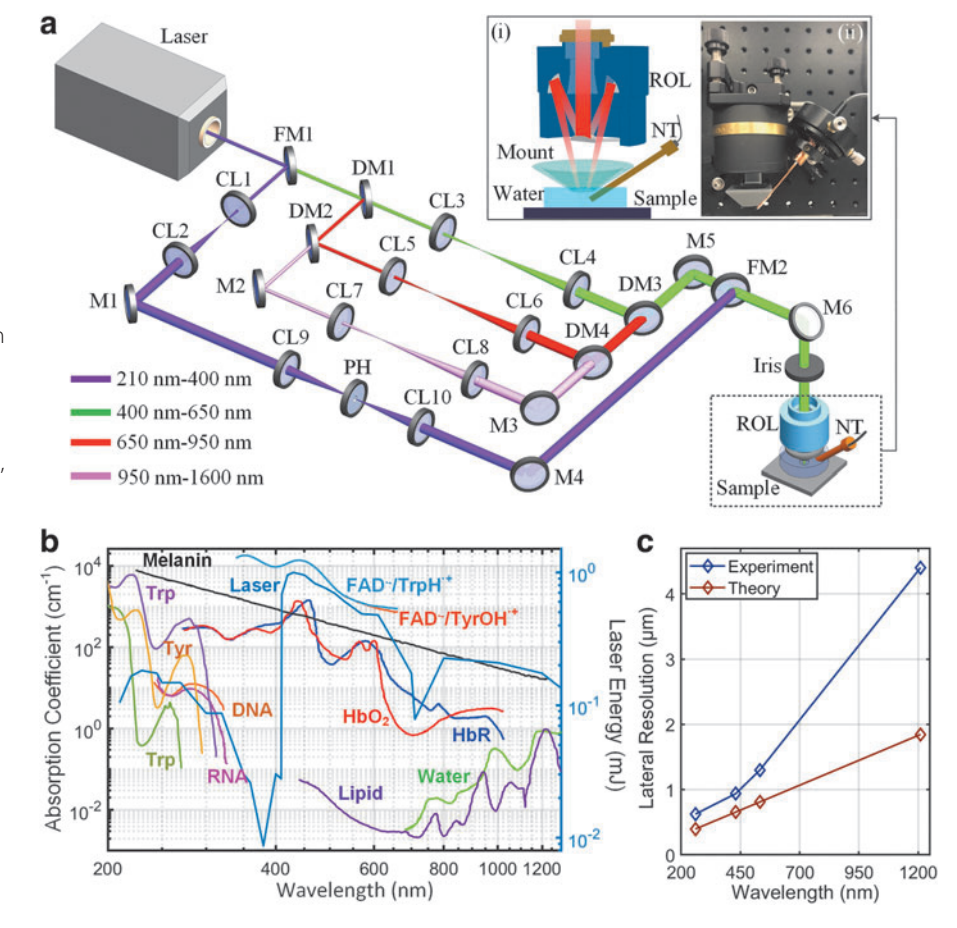
The small working distance reduces chromatic aberrations and absorption by the coupling water. The samples are translated using a high-precision three-axis motorized stage for volumetric imaging. The reflection-mode configuration allows for imaging organisms of different sizes. Details of the RHS-PAM system are provided in the Materials and Methods section.

The lateral resolution of RHS-PAM ranges from 0.625 to 4.4  $\mu$ m at representative absorbing wavelengths of cell nuclei, intracellular chromoproteins, hemoglobin, melanin, and lipids (Fig. 1c and Supplementary Fig. S2). For example, the lateral resolution at 266 nm was 0.625  $\mu$ m, which allows imaging subcellular components such as cell nuclei. The measured spatial resolution in the longer wavelength range was increasingly worse than the diffraction-limited theoretical estimation, mainly because of the nongaussian laser beam quality at longer wavelengths.

To highlight the advantage of the ROL-based system configuration, we also estimated the lateral spatial resolution of a

# FIG. 1. Schematic and characteristics of the RHS-PAM system.

- (a) Schematic of RHS-PAM system including four optical pathways with an illumination wavelength range of 210–1600 nm. Insets: (i) Sectional view illustration and (ii) photograph of the ROL and NT.
- **(b)** RHS-PAM laser output spectrum and absorption spectra of major tissue components, including DNA/RNA, HbR/HbO<sub>2</sub>, melanin, amino acid, flavoprotein, lipid, and water.<sup>31–35</sup>
- (c) Theoretical and measured lateral resolutions at four wavelengths (266, 430, 532, and 1210 nm). CL1–8, cylindrical convex lenses; DM1–4, dichroic mirrors; FM1–2, flip mirrors; M1–6, reflection mirrors; NT, needle transducer; PH, pinhole; RHS-PAM, reflection-mode hyperspectral photoacoustic microscopy; ROL, reflective objective lens.



traditional prism-based acoustic–optical beam-combiner used in PAM, and the results have clearly shown the severe chromatic aberration of the traditional setup (Supplementary Fig. S1). The NT has a frequency bandwidth of  $\sim\!40\,\mathrm{MHz}$  (Supplementary Fig. S3), which provides an axial resolution of  $\sim\!30\,\mu\mathrm{m}$  for RHS-PAM across the excitation spectrum.

# C. elegans imaging

*C. elegans* (or roundworm) is a transparent nematode ( $\sim$  1 mm in length) that lives in temperate soil environments. <sup>36,37</sup> Its transparent body consists of several layers: a body wall encompassing a collagenous cuticle, underlined by the hypodermis, nervous, and muscle systems; a pseudocoelome; and the internal organs of the alimentary and reproductive systems. *C. elegans* is a well-characterized animal model with known genome and desirable traits such as whole-body transparency, small size, fast growth rate, and ease of culturing. <sup>38</sup> Many genetic functions and biochemical pathways in *C. elegans* are shared with humans due to evolutionary conservation, making *C. elegans* a good model for investigating molecular pathways in human diseases.

In our study, a group of fixed *C. elegans* were imaged by RHS-PAM (Fig. 2a). Excited by 266 nm light, the epidermal layer of the worm was clearly visible with endogenous contrast of DNA/RNA and proteins (Fig. 2b). Unlike mammals, *C. elegans* does not have specialized adipose tissue. However, *C. elegans* intestinal cells and hypodermis may mimic the role of vertebrate adipocytes, having an analogous role as the main triglyceride depot.<sup>39,40</sup> Since triglycerides are triesters consisting of a glycerol molecule bound to

three fatty acid molecules that have strong UV light absorption,<sup>41</sup> it is believed that in addition to DNA/RAN and proteins, the image at 266 nm also contains lipids from the *C. elegans* hypodermis.

We then used 430 nm light for photoacoustic imaging of cytochrome-based or flavin-based contrasts. <sup>18</sup> At 430 nm, the whole body of *C. elegans* was imaged (Fig. 2c), and discrete structures can be differentiated, such as embryos ( $\sim$  30  $\mu$ m in diameter) distributed along one side of the body (Fig. 2d). <sup>42</sup> In addition, the body of *C. elegans* is rich in flavins, with a maximum absorption between 430 and 470 nm. <sup>43</sup> Flavins are present as prosthetic groups in flavoproteins and as cofactors in blue light photoreceptors, <sup>41,44</sup> and accumulate in *C. elegans* tissues in an oxidized form during aging. RHS-PAM at 430 nm can be used to map the distribution of endogenous flavins and cytochrome-based contrasts within the organism.

# In vivo frog tadpole imaging

Amphibian models have served important roles in developmental biology, 45-47 physiology, 48 genetics, 49,50 neurobiology, and toxicology. 54,55 Amphibian models are advantageous due to their large taxonomic diversity, well-understood internal phylogenetic relationships and basic physiology, and similarity to humans 48 (e.g., they are tetrapods and most are terrestrial 56). Adult frogs and tadpoles have been thoroughly investigated by multiple imaging modalities. 57-60 Photoacoustic imaging has proven useful for the study of glass frogs including the mechanism underlying their transparency, 61 and has been used to study tadpoles of different species. 14,62,63

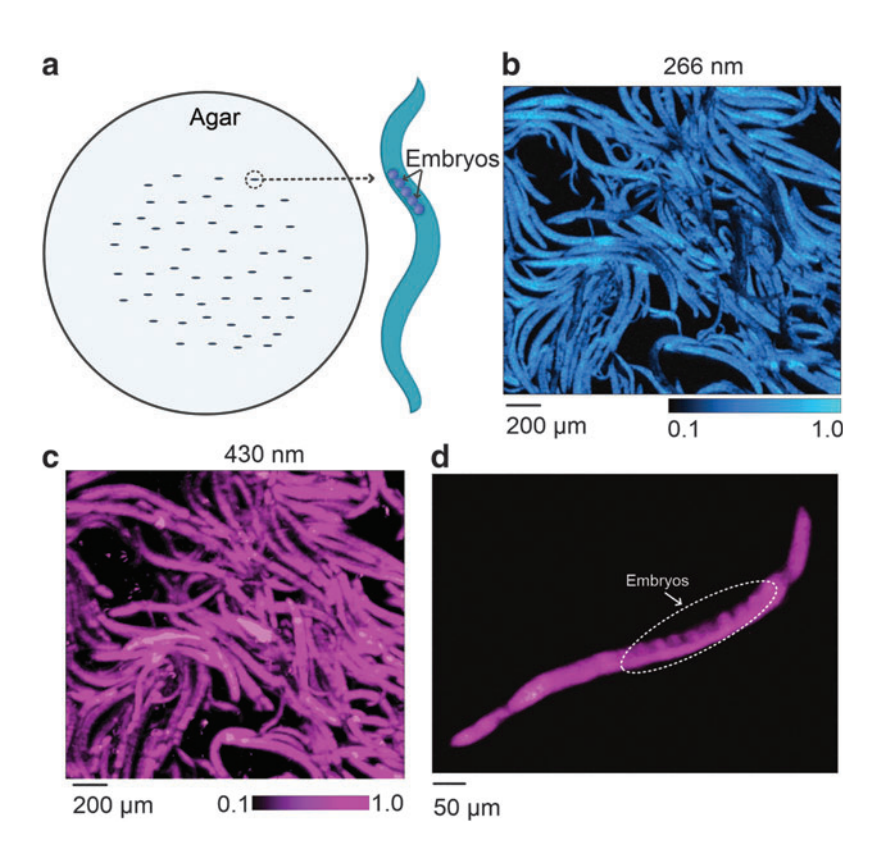


#### FIG. 2. RHS-PAM of Caenorhabditis elegans.

- (a) C. elegans were fixed in a 1% solid agar plate. RHS-PAM of C. elegans was conducted at 266 and 430 nm.
- **(b)** RHS-PAM of multiple *C. elegans* at 266 nm, showing the contrast from DNA/RNA and proteins
- **(c)** RHS-PAM of multiple *C. elegans* at 430 nm, showing the contrast from flavins.
- **(d)** Close-up image of a single *C. elegans* at 430 nm, showing the embryos.

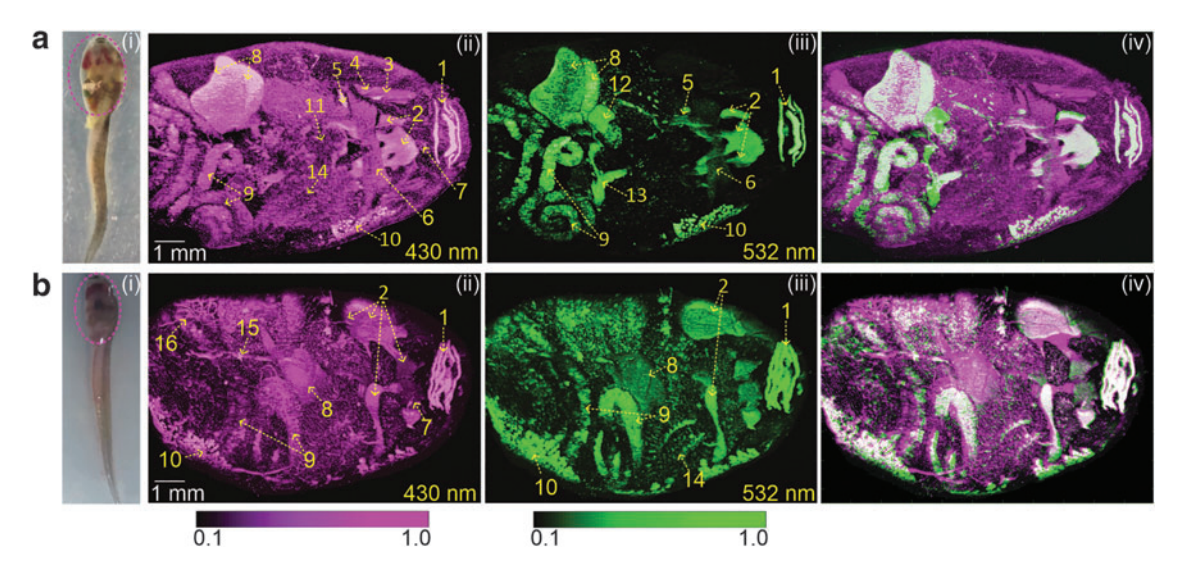


FIG. 3. RHS-PAM imaging of frog tadpoles (Teratohyla pulverata, Gossner Stage 28).

(a) RHS-PAM images at 430 and 532 nm, revealing skin and muscle vascularization and pigmentation.

**(b)** RHS-PAM images closer to the surface at 430 and 532 nm, revealing structures of internal organs, muscles, and blood vessels. (i) Photograph of a tadpole. The dashed oval boxes indicate the scanning area of the RHS-PAM images acquired at (ii) 430 nm, (iii) 532 nm, and (iv) merged images at two wavelengths. 1, keratinized labial teeth; 2, sinus hyobranchialis; 3–7, striated muscles (3, hyoangularis; 4, orbiotohyoideus; 5, subarqualis rectus; 6, interhyoideus; 7, intermandibularis); 8, liver lobes; 9, gut coils; 10, pigmentary cells (melanocytes); 11, heart; 12, gall bladder (biliverdin); 13, sinus venosus; 14, branchial basket; 15, abdominal vein; 16, skin vascularization.

In this section, we focused on extracting morphological features of tadpoles of the glass frog *Teratohyla pulverata*. Anesthetized tadpoles (Gossner Stage 28) were imaged *in vivo* at different depths from the ventral skin surface. The ventral side of tadpoles is transparent<sup>64,65</sup> (Fig. 3a-i, b-i), with a reduced concentration of pigments in their skin and muscles. This unique feature provides a natural window for imaging the internal organs. We targeted the main body of the tadpoles, excluding the tails. We chose two wavelengths of 430 and 532 nm. RHS-PAM at 430 nm targets abundant contrast agents such as yellow nitrogen-rich pteridines, <sup>66-68</sup> carotenoids, <sup>67</sup> the Soret band of porphyrins, and hemoglobin. <sup>69,70</sup>

Microanatomical features were extracted from the RHS-PAM images (Fig. 3a-ii, b-ii), including the oral apparatus (the black keratinized jaw sheaths and rows of teeth); skeletal muscle fibers from the interhyoideus, intermandibularis, hyoangularis, orbitohyoideus, rectus subarqualis muscles, and from the heart and gills; the hyobranchial sinus that collects and stores blood from the peripheral vascular system<sup>64</sup>; and in the abdominal area, the liver, long gut coils, gall bladder, and dermal melanophores bearing melanin granules and profuse skin vascularization in the images obtained at shallower depth (Fig. 3b-ii, iii).

The broad distribution of blue-absorbing pigments in extracellular fluids and lymph results in a reduced contrast between structures when imaged with 430 nm; therefore, the tadpoles were also imaged at a second wavelength, 532 nm. Because most endogenous proteins, pteridines, and carotenoids have weak absorption at 532 nm, RHS-PAM at this wavelength reveals

structures containing mostly hemoglobin and/or melanin (Fig. 3a-iii). <sup>5,8</sup> Using this approach, we acquired images of the hyobranchial sinus, branchial baskets, and the fine structure of hepatic lobes (Fig. 3a-iii, b-iii). The overlay images at 430 and 532 nm are shown in Figure 3a-iv and b-iv.

# Zebrafish imaging

Zebrafish is the most commonly used nonmammalian vertebrate animal model, and has proven valuable for the study of vertebrate development, gene function, and toxicology. The small body size and optical transparency of zebrafish larvae make them well suited for optical imaging. Traditional PAM techniques have been used to image the distribution of hemoglobin and analyze blood vessel types in zebrafish. Here, we used RHS-PAM to capture anatomical features of individual zebrafish at three developmental stages. To allow for longer imaging time, we used freshly preserved *ex vivo* specimens.

At 5 days postfertilization (5 dpf), zebrafish are transparent, which permits the transmission of light deep inside the organism (Fig. 4a). This transparency is especially important for RHS-PAM at short wavelengths, which are otherwise greatly attenuated by the outer skin layers. Figure 4b-i shows an *enface* projection of the zebrafish at 266 nm. Many morphological features are identifiable including the eye, brain, minor and major lobes of the medial fin fold, notochord, spinal cord, lateral line, myotomes, myosepta, otic capsule, intestine, and swim bladder. Different features were observed at 430 and 532 nm

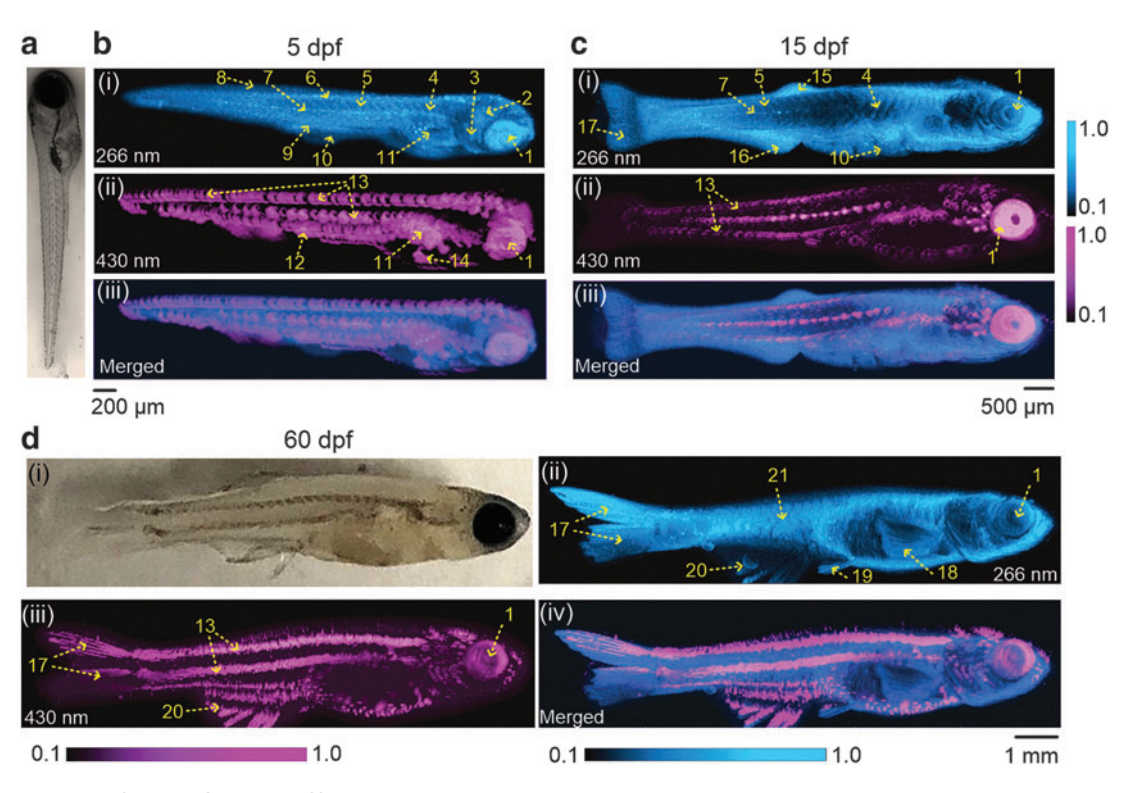


FIG. 4. RHS-PAM of zebrafish at different developmental stages.

(a) Photograph of a 5 dpf zebrafish.

**(b, c)** RHS-PAM images of zebrafish at 5 dpf **(b)** and 15 dpf **(c)** at (i) 266 nm, (ii) 430 nm, and (iii) merged image at two wavelengths. **(d)** (i) Photograph of a 60 dpf zebrafish. RHS-PAM images of the 60 dpf zebrafish at (ii) 266 nm, (iii) 430 nm, and (iv) merged image at two wavelengths. 1, eye; 2, brain; 3, otic capsule; 4, myoseptum; 5, myotomes; 6, melanocytes; 7, notochord; 8, median fin fold; 9, intestine; 10, minor lobe of the median fin fold; 11, swim bladder; 12, intestine; 13, intersegmental vessels; 14, heart; 15, dorsal fin fold; 16, anal fin fold; 17, caudal fin, pelvic fin; 18, pectoral fin; 19, pelvic fin; 20, anal fin; 21, scales. dpf, days postfertilization.

(Fig. 4b-ii and Supplementary Fig. S4a). Images at these two wavelengths depict similar morphological features, including the heart, intersegmental vessels, and swimming bladder, outlined by melanocytes.

At 15 dpf, larger myotomes and myosepta, distinctive dorsal and anal fin folds, and caudal fin are observed at 266 nm (Fig. 4c-i). At 430 and 532 nm, trunk intersegmental vessels are revealed (Fig. 4c-ii and Supplementary Fig. S4b).

Juvenile zebrafish (30–90 dpf) are characterized by a transformation of their fins, including complete loss of the larval fin fold and development of the caudal, anal, pelvic, dorsal, and pectoral fins. The skin of juvenile zebrafish also shows a complete pattern of scales (squamation).<sup>75</sup> Similar to amniote skin appendages, zebrafish scales develop relatively late in ontogeny and are distributed across the skin.<sup>76,77</sup> These elasmoid scales are made of dermal bone embedded in the skin with strong absorption in the UV range.<sup>78</sup>

We imaged a 60 dpf juvenile zebrafish at 266 nm, which revealed a complete squamation pattern across the entire body surface, showing the characteristic overlapping shingle-like pattern (Fig. 4d-i, d-ii). Similar to larval zebrafish images at 266 nm, because various molecules have absorption in the deep UV band, other morphological features are also observed,

including melanin in the eyes, and the dorsal, anal, pelvic pectoral, and caudal fins. At longer wavelengths of 430 and 532 nm, we observed the development of the pigment pattern of juveniles and adults, including the characteristic melanophore stripes in the flanks of the body (Fig. 4d-iii and Supplementary Fig. S4c).

# Mouse brain and ear imaging

Mice have long been used as models of neuroscience and neurology because of their phylogenetic proximity and physiological similarity to humans, and the ease of maintaining them in the laboratory. Mouse models have been used to study brain disease pathologies and to evaluate the effectiveness of treatments. However, most research has to use histological analysis with exogenous labeling.

In this study, we focused on a mouse brain model of ischemic stroke.  $^{80,81}$  Different morphological features of the brain contain different endogenous biomolecules with unique light absorption spectra, such as nuclei, hemoglobin, and lipids,  $^{31,80}$  providing rich contrast between microanatomical structures, such as caudoputamen, third ventricle, and hippocampus.  $^{8,16}$  We analyzed coronal sections (100  $\mu \rm m$  thickness) from a mouse brain

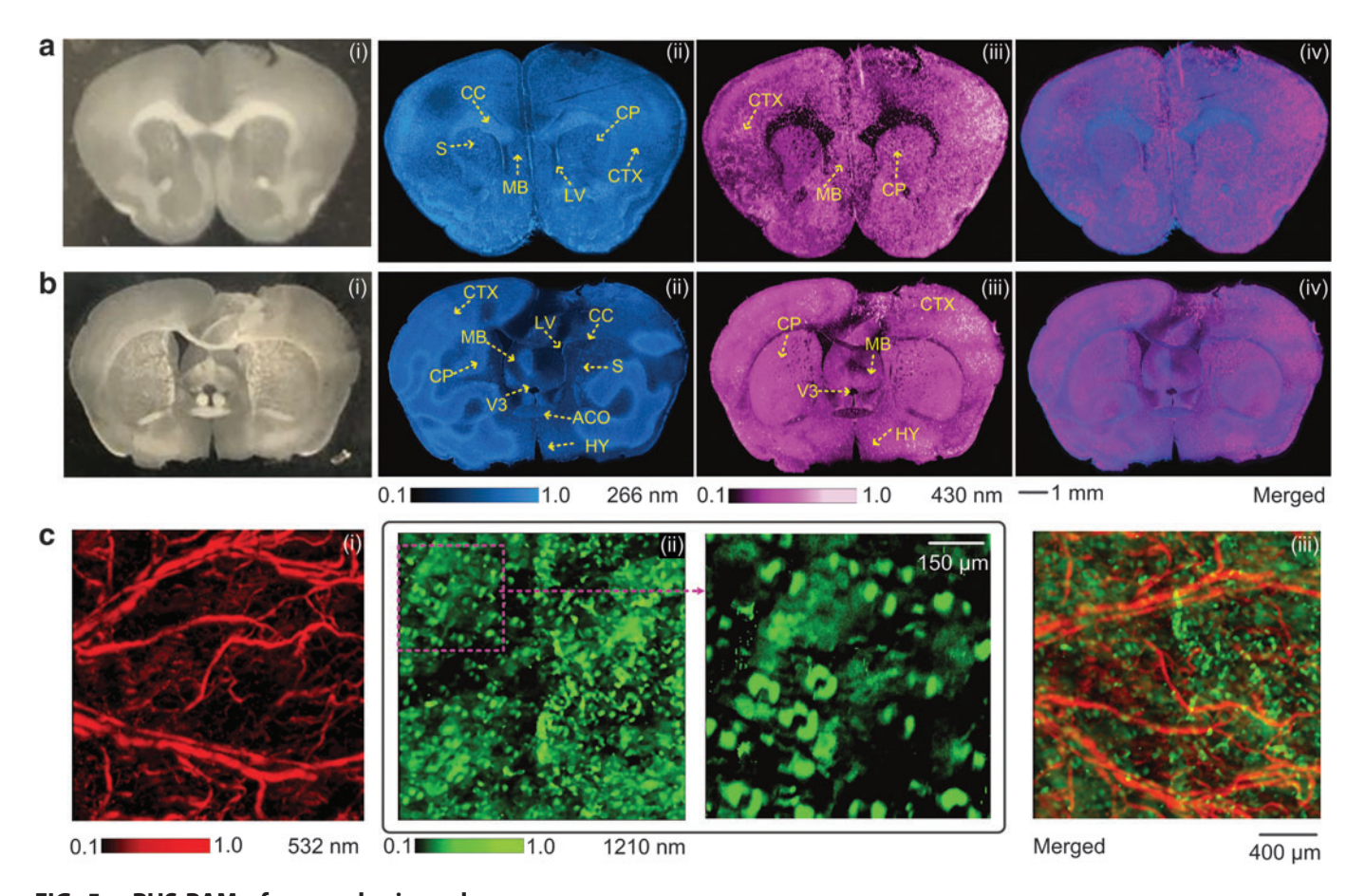


FIG. 5. RHS-PAM of mouse brain and ear.

(a, b) RHS-PAM of two coronal sections of anterior mouse brain with ischemic stroke. (i) Wide-field photographs of coronal sections, (ii) RHS-PAM images at 266 nm, (iii) RHS-PAM images at 430 nm, and (iv) merged RHS-PAM images at two wavelengths.

(c) RHS-PAM of the mouse ear. (i) RHS-PAM image of blood vessels at 532 nm, (ii) RHS-PAM image of sebaceous glands at 1210 nm, and close-up image of glands, (iii) merged image at two wavelengths (red channel: 532 nm; green channel: 1210 nm). ACO, anterior commissure; CC, corpus callosum; CP, caudate putamen; CTX, cerebral cortex; HY, hypothalamus; LV, lateral ventricle; MB, midbrain; S, striatum; V3, third ventricle.

subjected to photothrombotic stroke (1 day after stroke) on the right (ipsilateral [IL]) hemisphere.

RHS-PAM was used to image nuclei and protein at 266 nm, as well as hemoglobin and melanin at 430 nm (Fig. 5a, b). <sup>18</sup> Various morphological features were identifiable at these two wavelengths. Images at 266 nm revealed the lateral ventricles, striatum, third ventricle, corpus callosum, cerebral cortex, anterior commissure, midbrain, and hippocampus (Fig. 5a-i, b-i). The subcellular resolution of RHS-PAM at 266 nm also allows for the detection of cell nuclei (Supplementary Fig. S5). Because of the stroke-induced hypoxia, some cells within the affected region die, reducing the number of cell nuclei within the IL hemisphere relative to the uninjured contralateral (CL) hemisphere.

By analyzing the averaged signal intensity of both hemispheres (Supplementary Fig. S6), we observed lower signal intensities within the IL hemisphere (93.0 in the anterior section, 74.7 in the posterior section), compared with the CL hemisphere (99.4 in the anterior section, 87.5 in the posterior section). The

signal intensity difference is consistent with the expected reduction in the number of cells in the IL hemisphere. Interestingly, images at 430 nm produced greater signal intensity in the IL hemisphere (155.7 in the anterior section, 171.4 in the posterior section) than in the CL hemisphere (137.5 in the anterior section, 167.2 in the posterior section) (Fig. 5a-i, b-ii and Supplementary Fig. S6).

These increased intensities within the IL hemisphere could represent the immune cells infiltration due to the stroke, as well as the increase in the presence of proteins like hemoglobin. In photothrombotic stroke, some of the blood vessels would be broken due to the thrombi, the brain–blood barrier is then compromised ("broken"), and there is infiltration of cells/blood from the blood into the brain region with stroke.

Mouse ear has a dense supply of blood vessels and sebaceous glands in the dermis of the skin, and is a commonly used skin model. We imaged a mouse ear *in vivo* with illumination at 532 and 1210 nm. RHS-PAM at 532 nm was used to image

hemoglobin in the vascular system in the ear (Fig. 5c-i). The same region of the ear was then imaged at 1210 nm, which is an absorption peak of lipids (Fig. 1b). Sebaceous glands were observed in the dermis (Fig. 5c-ii).

The images allowed the identification of alveoli of the holocrine sebaceous glands. When imaging deeper region of the ear, in addition to sebaceous glands, subcutaneous and periaortic fat were also observed (Supplementary Fig. S7). An overlay image at 532 and 1210 nm is shown in Figure 5c-iii. Blood vessels (red) and sebaceous glands (green) were clearly imaged in the middermis.

#### **Discussion**

We thoroughly investigated the performance of the RHS-PAM system. The measured lateral resolutions are larger than the theoretical values, especially at longer wavelengths such as 1210 nm. This resolution difference is primarily due to the poor beam quality of the broadband laser at longer wavelengths. Short wavelength excitation (e.g., 266 and 430 nm) is needed for probing subcellular morphology, and thus the system was tuned to improve the beam quality at these wavelengths. Although the system has a relatively low lateral resolution at 1210 nm, it still allows imaging lipid-rich sebaceous glands with  $\sim 5\,\mu{\rm m}$  resolution and identifying cellular-level components.

Future efforts are needed to improve the laser beam quality for a broader wavelength range. The axial resolution can be improved by optimizing the transducer's frequency performance. The ROL has two hemispherical mirrors that enable low chromatic aberration over a broadband spectral range, achieving the same focal length for a wide spectral range. A thin layer of water was needed to immerse the NT, which is  $\sim\!1$  mm to the sample surface. The small working distance of the NT can reduce the loss of high-frequency photoacoustic signals and improve the detection sensitivity.

Several technical shortcomings are directly resultant from the low imaging speed, which is currently limited by the excitation laser's pulse repetition rate of 100 Hz and its slow wavelength tuning. First, we were not able to provide the comprehensive absorption spectra of the imaged targets over a broad wavelength range, but rather at a few representative wavelengths. Second, we were not able to provide quantitative spectral analysis or ratiometric measurement of different tissue components, but rather a qualitative mapping of the dominating tissue components at selected wavelengths.

In future study, an advanced laser with supercontinuum wavelength output and fast wavelength tuning can improve the imaging speed, and allow for more wavelengths to be used for spectrally unmixing chromophores with overlapping absorption spectra. Moreover, advanced computational image processing and cell segmentation approaches are needed to provide spatially resolved single-cell-level biochemical profiles.

With these technical improvements, we expect that RHS-PAM will find increasing applications in biomedical research such as diagnosis of skin diseases, quantitative analysis of tissue metabolites, and image-guided tumor margin assessment.<sup>82–84</sup>

# The Bigger Picture

Our initial success with the RHS-PAM system offers encouraging insights into its capabilities for detailed structural and molecular imaging in diverse animal models. This study provides a foundation for the broader applications of label-free microscopic assessment of biological materials.

As we look to the future, the RHS-PAM system stands to benefit from targeted technical refinements, allowing for tailored optimization depending on the specific application needs. Beyond its utility for endogenous contrast imaging, the system also has the capacity to integrate a wide range of chromophore-specific exogenous contrast agents, leveraging work already done in other absorption-based imaging methods.

Building on this promise, we are optimistic about the role RHS-PAM could play in the evolving field of label-free single-cell biochemical mapping. With further technological advancements, we anticipate that RHS-PAM may ultimately offer clinicians and patients a more objective noninvasive way to obtain cellular-level spatial omics, potentially enriching diagnostic and treatment pathways.

#### **Conclusion**

In this study, we have implemented an RHS-PAM system with an ROL and a miniaturized NT. This RHS-PAM system can probe a variety of endogenous biomolecules on thick samples or *in vivo*, with high spatial resolutions across the spectral range from UV to NIR. Using RHS-PAM, we studied several model organisms *in vitro* or *in vivo*—C. *elegans*, frog tadpoles, zebrafish, and mouse. RHS-PAM identified anatomical features of these models, using endogenous contrasts such as DNA/RNA, proteins, hemoglobin, and lipids, without the need for labeling or staining. Our results have demonstrated that RHS-PAM has a great potential for label-free imaging of a broad range of endogenous contrasts.

# **Materials and Methods**

#### **RHS-PAM system**

The system consists of a wavelength-tunable laser (Q-TUNE-C100-SH-AT, wavelength range: 210–2300 nm; pulse repetition frequency: 100 Hz). The output power of the laser was controlled by a variable attenuator. A flip mirror was used to select the UV wavelength band from 210 to 400 nm. A pair of cylindrical lenses was used to reshape the light beam due to the elliptical laser output, and a spatial filter was implemented by using a pair of achromatic convex lens and a pinhole (P15C; Thorlabs). The longer wavelength was passed through two dichroic mirrors (DMSP650L and DMLP950L) to separate three wavelength bands (400–650, 650–950, and >950 nm).

In this way, we managed each wavelength band with appropriate achromatic optic systems and beam reshaping. Another set of the same series of dichroic mirrors was used to recombine the excitation pathways. Final focusing of all beam pathways onto the samples was provided by an ROL (50105-02; Newport) coated with UV-enhanced aluminum, with zero chromatic aberration over a broad spectral range (200–20,000 nm) and a numeric aperture of 0.4. A small water tank was mounted under the ROL. The bottom of the tank was sealed with a UV-fused silica broadband window (WG40530; Thorlabs).

A NT with a center frequency of 35 MHz and bandwidth  $\sim\!43\,\text{MHz}$  (Supplementary Fig. S3) was used to detect the photoacoustic signals. To reduce the acoustic transmission loss, the NT detection face was close to the sample, at a distance of  $\sim\!1\,\text{mm}$ . Mechanical scanning of the sample was provided by the linear stepper motor stages (L-509.10SD00; Physik Instrument). The signals were amplified and digitized by a data acquisition card (ATS9350; Alazar Technologies). In data process, a slight thresholding was also applied to the images to remove excessive background signals, mostly from the coupling medium. A 2D 3 by 3 median filter was used to improve the image contrast. A binary mask was applied to the brain slice images.

#### **Resolution measurement**

The lateral resolution of the RHS-PAM system was characterized at different wavelengths. For each measurement, the edge spread function (ESF) was obtained by repeatedly scanning a sharp edge of a resolution target (R3L3S1P; Thorlabs, Inc.) 30 times with a step size of 0.3125  $\mu m$  (blue dashed curve in Fig. 2). The corresponding line spread function (LSF) was calculated by taking the first derivative of the ESF (red curve in Fig. 2). We calculated the full width at half maximum of the LSF as the lateral resolution.

#### Preparation of animal models

All animal procedures were approved by the Duke University Medical Center Animal Care and Use Committee (Protocol numbers: A174-21-08, A009-20-01) and were conducted in accordance with the United States Public Health Service's Policy on Humane Care and Use of Laboratory Animals.

# Caenorhabditis elegans

C. elegans roundworms were fixed in 4% paraformaldehyde in phosphate buffered saline (PBS) overnight at 4°C, and were washed three times with PBS and placed in a Petri dish for imaging. Fixed worms were detached from the dish using deionized water and a dropper pipe and kept in  $\sim 1\,\mathrm{mL}$  of water. To fix the C. elegans position on the dish, a 1% solid agar plate (<1 mm thickness) was placed to cover the roundworms, and any air bubbles were removed to avoid artifacts. To keep the sample in water during imaging, the gap between agar plate and dish was sealed using a low-melting point agar liquid (BCBZ6858; Sigma-Aldrich).

#### Frog tadpoles

Two *T. pulverata* tadpoles (Gossner stage 28) were analyzed. The tadpoles were anesthetized by immersion in 0.35 g/L tricaine methanesulfonate solution (MS-222; Sigma-Aldrich). Each tadpole's tail was immersed in 1% low-melting point agar in supine position exposing the abdomen. The reduced pigment in the tadpole's abdominal skin makes this area an ideal window for imaging. The agar was solidified, limiting the rotation and translation of the tadpoles while imaging. The body surface was covered by a thin layer of water for acoustic coupling.

#### Mouse brain sections

Male and female C57Bl/6 mice (3–6 months old) were used. A photothrombotic stroke was performed as described previously. Mice were anesthetized using a face mask and inhalation of 1.5% isoflurane in 30% oxygen and 70% nitrogen. The animal was placed in a stereotaxic frame and the body temperature was maintained at  $37.0^{\circ}\text{C}\pm0.5^{\circ}\text{C}$  by using a recirculating water heating pad. The skull was exposed by a dorsal midline incision (  $\sim$  1.3 cm) and Rose Bengal

(10 mg/mL in saline, 0.1 mg per gram of body weight) was administered intraperitoneally. A cold green light with a 2.5 mm spot size was placed at 1.5 mm from the bregma.

Five minutes after the Rose Bengal injection, the green light was turned on to induce cortical vessel occlusion by illumination for 15 min through the intact skull. Skin incisions were closed using interrupted nylon sutures and local antibiotic ointment was applied on the incision. The animal was removed from the stereotaxic frame and monitored for 2 h at 32°C before being returned to its home cage. Food and water were provided ad libitum. At 1 day poststroke, the brain samples were harvested after cardiac perfusion with PBS followed by 4% (v/v) paraformaldehyde in PBS.

Samples were postfixated overnight at 4°C in 4% PFA, and sectioned at a thickness of  $\sim 100~\mu m$  using a vibratome (VT1000P; Leica Microsystems, Wetzlar, Germany). Coronal sections were collected in PBS and kept at 4°C until analysis (stored for a maximum of 4 weeks). For imaging, fixed brain slices were placed on glass slides and flattened under the optical microscope. A 1% solid agar plate was used to overlay the surface of the brain slice and fix it. Two coronal slices from an anterior position (including lateral ventricles) and from a posterior position (including the hippocampus) were analyzed. The samples were placed in a water tank and scanned.

#### Zebrafish

Wild-type (Ekkwill) zebrafish were imaged at larval and juvenile stages (5, 15, and 60 dpf). Zebrafish were housed in a recirculating AHAB system (Aquatic Habitats, Apopka, FL) at 28°C under a 14-h cycle: 10 h light: 4 h dark. Larval zebrafish were spawned by paired breeding and were reared in Danieau's embryo medium. Zebrafish were euthanized by rapid submersion in ice water and fixation in 10% neutral buffered formalin.

#### Mouse ear

For mouse ear imaging, the mouse was anesthetized with 1.0–1.5% v/v isoflurane and kept warm at 37°C using a heating pad. The mouse's ear was held on a flat glass holder and covered with ultrasound gel for acoustic coupling. A small area of 2×2 mm was imaged at 532 and 1210 nm. The laser beam focal zone was positioned  $\sim$  20  $\mu m$  deeper when using 1210 nm to image the sebaceous glands under the ear skin.

#### **Authors' Contributions**

Q.R. constructed the RHS-PAM system and performed all the imaging experiments and data analysis. C.T., I.M., and N.J. assisted with *C. elegans*, frog tadpole, and zebrafish models, and data analysis. A.d.A., and W.Y. assisted with mouse brain sections and the corresponding data analysis. Y.Z., and Q.Z. fabricated the NT and characterized its performance. J.Y. supervised the whole project. Q.R., C.T., and J.Y. wrote the article. All authors reviewed and revised the article.

#### **Author Disclosure Statement**

No competing financial interests exist.

#### **Funding Information**

This study was supported by grants EB028143, NS111039, and NS115581 from the U.S. National Institutes of Health, CAREER award 2144788 from the U.S. National Science Foundation, and 226178 from the Chan Zuckerberg Initiative, all to J.Y.

# **Supplementary Material**

Supplementary Figure S1

Supplementary Figure S2

Supplementary Figure S3

Supplementary Figure S4

Supplementary Figure S5

Supplementary Figure S6

Supplementary Figure S7

#### References

- Fan JL, Rivera JA, Sun W, et al. High-speed volumetric two-photon fluorescence imaging of neurovascular dynamics. Nat Commun 2020;11(1):6020; doi: 10.1038/s41467-020-19851-1
- Johnstonbaugh K, Agrawal S, Durairaj DA, et al. A deep learning approach to photoacoustic wavefront localization in deep-tissue medium. IEEE Trans Ultrason Ferroelectr Freq Control 2020;67(12):2649–2659; doi: 10.1109/ TUFFC.2020.2964698
- Bi Y, Yang C, Chen Y, et al. Near-resonance enhanced label-free stimulated Raman scattering microscopy with spatial resolution near 130 nm. Light Sci Appl 2018;7:81; doi: 10.1038/s41377-018-0082-1
- Ortega S, Halicek M, Fabelo H, et al. Hyperspectral and multispectral imaging in digital and computational pathology: A systematic review. Biomed Opt Express 2020;11(6):3195–3233; doi: 10.1364/BOE.386338
- Nam HS, Kang WJ, Lee MW, et al. Multispectral analog-mean-delay fluorescence lifetime imaging combined with optical coherence tomography. Biomed Opt Express 2018;9(4):1930–1947; doi: 10.1364/BOE.9.001930
- Hu Z, Fang C, Li B, et al. First-in-human liver-tumour surgery guided by multispectral fluorescence imaging in the visible and near-infrared-l/ll windows. Nat Biomed Eng 2020;4(3):259–271; doi: 10.1038/s41551-019-0494-0
- Bea SM, Bae DJ, Do EJ, et al. Multi-spectral fluorescence imaging of colon dysplasia in vivo using a multi-spectral endoscopy system. Transl Oncol 2019;12(2):226–235; doi: 10.1016/j.tranon.2018.10.006
- Abdeladim L, Matho KS, Clavreul S, et al. Multicolor multiscale brain imaging with chromatic multiphoton serial microscopy. Nat Commun 2019;10(1):1662; doi: 10.1038/s41467-019-09552-9
- Cho SW, Park SM, Park B, et al. High-speed photoacoustic microscopy: A review dedicated on light sources, Photoacoustics 2021;24:100291; doi:10 .1016/j.pacs.2021. 100291
- Kim J, Kim JY, Jeon S, et al. Super-resolution localization photoacoustic microscopy using intrinsic red blood cells as contrast absorbers. Light Sci Appl 2019;8:103; doi: 10.1038/s41377-019-0220-4
- Chena J, Zhang Y, Heb L, et al. Wide-field polygon-scanning photoacoustic microscopy of oxygen saturation at 1-MHz A-line rate. Photoacoustics 2020;20:100195; doi: 10.1016/j.pacs.2020.100195
- Li X., Kang L, Zhang Y, et al. High-speed label-free ultraviolet photoacoustic microscopy for histology-like imaging of unprocessed biological tissues. Opt Lett 2020;45(19):5401–5404; doi: 10.1364/OL.401643
- Lee H, Seeger MR, Lippok N, et al. Nanosecond SRS fiber amplifier for labelfree near-infrared photoacoustic microscopy of lipids. Photoacoustics 2022;25:100331; doi: 10.1016/j.pacs.2022.100331
- Dasaa MK, Nterolid G, Bowenc P, et al. All-fibre supercontinuum laser for in vivo multispectral photoacoustic microscopy of lipids in the extended near-infrared region. Photoacoustics 2020;18:100163; doi: 10.1016/j.pacs .2020.100163
- Yang W, Wang W, Jing L, et al. Label-free photoacoustic microscopy: A potential tool for the live imaging of blood disorders in zebrafish. Biomed Opt Express 2021;12(6):3643–3657; doi: 10.1364/BOE.425994
- Wong TTW, Zhang R, Zhang C, et al. Label-free automated threedimensional imaging of whole organs by microtomy-assisted photoacoustic microscopy. Nat Commun 2017;8(1):1386; doi: 10.1038/ s41467-017-01649-3
- Wang K, Li C, Chen R, et al. Recent advances in high-speed photoacoustic microscopy. Photoacoustics 2021;24:100294; doi: 10.1016/j.pacs.2021 100294
- Baik J W, Kim H, Son M, et al. Intraoperative label-free photoacoustic histopathology of clinical specimens. Laser Photonics Rev 2021;15(10); doi: 10 .1002/lpor.202100124
- Yao DK, Chen R, Maslov K, et al. Optimal ultraviolet wavelength for in vivo photoacoustic imaging of cell nuclei. J Biomed Opt 2012;17(5):056004; doi: 10.1117/1JBO.17.5.056004

- Imai T, Shi J, Wong TTW, et al. High-throughput ultraviolet photoacoustic microscopy with multifocal excitation. J Biomed Opt 2018;23(3):1–6; doi: 10 .1117/1.JBO.23.3.036007
- Cao R, Tran A, Li J, et al. Hemodynamic and oxygen-metabolic responses of the awake mouse brain to hypercapnia revealed by multiparametric photoacoustic microscopy. J Cereb Blood Flow Metab 2021;41(10):2628– 2639; doi: 10.1177/0271678X211010352
- Qin W, Jin T, Guo H, et al. Large-field-of-view optical resolution photoacoustic microscopy. Opt Express 2018;26(4):4271–4278; doi: 10.1364/OE.26.004271
- He Y, Shi J, Pleitez MA, et al. Label-free imaging of lipid-rich biological tissues by mid-infrared photoacoustic microscopy. J Biomed Opt 2020;25(10):106506; doi: 10.1117/1.JBO.25.10.106506
- Pleitez MA, Khan AA, Soldà A, et al. Label-free metabolic imaging by midinfrared optoacoustic microscopy in living cells. Nat Biotechnol 2020;38(3):293–296; doi: 10.1038/s41587-019-0359-9
- Bell K, Mukhangaliyeva L, Khalili L, et al. Hyperspectral absorption microscopy using photoacoustic remote sensing. Opt Express 2021;29(15):24338– 24348; doi: 10.1364/OE.430403
- Park SM, Kim DY, Cho SW, et al. Quickly alternating green and red laser source for real-time multispectral photoacoustic microscopy. Photoacoustics 2020;20:100204; doi: 10.1016/j.pacs.2020.100204
- Cao R, Kilroy JP, Ning B, et al. Multispectral photoacoustic microscopy based on an optical–acoustic objective. Photoacoustics 2015;3(2):55–59; doi: 10 .1016/j.pacs. 2014.12.004
- Ecclestone BR, Bell K, Sparkes S, et al. Label-free complete absorption microscopy using second generation photoacoustic remote sensing. Sci Rep 2022;12(1):8464; doi: 10.1038/s41598-022-11235-3
- Hu S, Maslov K, Wang LV. Second-generation optical-resolution photoacoustic microscopy with improved sensitivity and speed. Opt Lett 2011;36(7):1134–1136; doi: 10.1364/OL.36.001134
- Hajireza P, Shi W, Zemp RJ. Real-time handheld optical-resolution photoacoustic microscopy. Opt Express 2011;19(21):20097–20102; doi: 10.1364/OE .19.020097
- Oliveira LMCO, Tuchin VV. The optical clearing method—A new tool for clinical practice and biomedical engineering. SpringerBriefs in Physics, 2019; doi: 10.1007/978-3-030-33055-2.
- Dasa MK, Markos C, Maria M, et al. High-pulse energy supercontinuum laser for high-resolution spectroscopic photoacoustic imaging of lipids in the 1650–1850 nm region. Biomed Opt Express 2018;9(4):1762–1770; doi: 10 .1364/BOE.9.001762
- 33. Kumar NV, Govil G. Theoretical studies on protein–nucleic acid interactions. III. Stacking of aromatic amino acids with bases and base pairs of nucleic acids. Biopolymers 1984;23(10):2009–2024; doi: 10.1002/bip.360231015
- 34. Jakubowski H, Flatt P. Map: Principles of Biochemistry (Lehninger). LibreTexts Biology: Arlington, TX; 2023; pp. 127–128.
- 35. Zhuang B, Seo D, Aleksandrov A, et al. Characterization of light-induced, short-lived interacting radicals in the active site of flavoprotein ferredoxin-NADP+ oxidoreductase. J Am Chem Soc 2021;143:2757–2768; doi: 10.1021/iasc.0c006.27
- 36. Mohrlen F, Hutter H, Zwilling R. The astacin protein family in *Caenorhabditis elegans*. Eur J Biochem 2003;270(24):4909–4920; doi: 10.1046/j.1432-1033 .2003.03891.x
- Loer CM, Kenyon CJ. Serotonin-deficient mutants and male mating behavior in the nematode *Caenorhabditis elegans*. J Neurosci 1993;13(12):5407–5417; doi: 10.1523/JNEUROSCI.13-12-05407.1993
- Poupet C, Chassard C, Nivoliez A, et al. Caenorhabditis elegans, a host to investigate the probiotic properties of beneficial microorganisms, Front Nutr 2020:7:135: doi: 10.3389/fnut.2020.00135
- Lemieux GA, Ashrafi K. Investigating connections between metabolism, longevity, and behavior in *Caenorhabditis elegans*. Trends Endocrinol Metab 2016;27(8):586–596; doi: 10.1016/j.tem.2016.05.004
- Yu CC, Barry NC, Wassie AT, et al. Expansion microscopy of C. elegans. Elife 2020;9:e46249; doi: 10.7554/eLife.46249
- 41. Espada L, Dakhovnik A, Chaudhari P, et al. Loss of metabolic plasticity underlies metformin toxicity in aged *Caenorhabditis elegans*. Nat Metab 2020;2(11):1316–1331; doi: 10.1038/s42255-020-00307-1
- Marré J, Traver EC, Jose AM. Extracellular RNA is transported from one generation to the next in *Caenorhabditis elegans*. Natl Acad Sci 2016;113(44):12496–12501; doi: 10.1073/pnas.1608959113
- Nedosekin DA, Galanzha El, Ayyadevara S, et al. Photothermal confocal spectromicroscopy of multiple cellular chromophores and fluorophores. Biophys J 2012;102(3):672–681; doi: 10.1016/j.bpj.2011.12.035

- Davis Jr BO, Anderson GL, Dusenbery DB. Total luminescence spectroscopy of fluorescence changes during aging in *Caenorhabditis elegans*. Biochemistry 1982;21(17):4089–4095; doi: 10.1021/bi00260a027
- 45. Tata JR. Amphibian metamorphosis as a model for the developmental actions of thyroid hormone. Mol Cell Endocrinol 2006;246(1–2):10–20; doi: 10.1016/j. mce.2005.11.024
- Voss S R, Epperlein HH, Tanaka EM. Ambystoma mexicanum, the axolotl: A versatile amphibian model for regeneration, development, and evolution studies. Cold Spring Harb Protoc 2009;2009(8):pdb.emo128; doi: 10.1101/ pdb.emo128
- 47. Bolker JA. Model systems in developmental biology. BioEssays 1995;17(5):451–455; doi: 10.1002/bies.950170513
- Burggren WW, Warburton S. Amphibians as animal models for laboratory research in physiology. ILAR J 2007;48(3):260–269; doi: 10.1093/ilar.48.3.260
- Hartley KO, Hardcastle Z, Friday RV, et al. Transgenic Xenopus embryos reveal that anterior neural development requires continued suppression of BMP signaling after gastrulation. Dev Biol 2001;238(1):168–184; doi: 10.1006/ dbio.2001.0398
- 50. Harland RM, Grainger RM. Xenopus research: Metamorphosed by genetics and genomics. Trends Genet 2011;27(12):507–515; doi: 10.1016/j.tig.2011 08.003
- 51. lyer AA, Briggman KL. Amphibian behavioral diversity offers insights into evolutionary neurobiology. Curr Opin Neurobiol 2021;71:19–28; doi:10 .1016/j.conb. 2021.07.015
- 52. Northcutt RG, Kicliter E. Organization of the amphibian telencephalon. In: Comparative Neurology of the Telencephalon 1980;203–255; doi: 10.1007/978-1-4613-2988-6\_8
- 53. Wilczynski W, Ryan MJ. The behavioral neuroscience of anuran social signal processing. Curr Opin Neurobiol 2010;20(6):754–763; doi: 10.1016/j.conb. 2010.08.021
- Hopkins WA. Amphibians as models for studying environmental change. ILAR J 2007;48(3):270–277; doi: 10.1093/ilar.48.3.270
- Kloas W. Amphibians as a model for the study of endocrine disruptors. Int Rev Cytol 2002;216:1–57; doi: 10.1016/s0074-7696(02)16002-5
- MacIver MA, Schmitz L, Mugan U, et al. Massive increase in visual range preceded the origin of terrestrial vertebrates. Natl Acad Sci 2017;114(12):E2375–E2384; doi: 10.1073/pnas.1615563114
- Boppart SA, Tearney GJ, Bouma BE, et al. Noninvasive assessment of the developing Xenopus cardiovascular system using optical coherence tomography. Proc Natl Acad Sci U S A 1997;94(9):4256–4261; doi: 10.1073/ pnas.94.9.4256
- Rubinsky B, Wong ST, Hong JS, et al. 1H magnetic resonance imaging of freezing and thawing in freeze-tolerant frogs. Am J Physiol Regul Integr Comp Physiol 1994;266(6Pt2):R1771–R1777; doi: 10.1152/ajpregu.1994. 266.6.R1771
- Taboada C, Brunetti AE, Pedron FN, et al. Naturally occurring fluorescence in frogs, Proc Natl Acad Sci U S A 2017;114(14):3672–3677; doi: 10.1073/pnas .1701053114
- Kolker SJ, Tajchman U, Weeks DL. Confocal imaging of early heart development in Xenopus laevis. Dev Biol 2000;218(1):64–73; doi: 10.1006/dbio. 1999.9558
- 61. Taboada C, Delia J, Chen M, et al. Glassfrogs conceal blood in their liver to maintain transparency. Science 2022;378(6626):1315–1320; doi: 10.1126/
- Rong Q, Lee Y, Tang Y, et al. High-frequency 3D photoacoustic computed tomography using an optical microring resonator. BME Front 2022;2022:9891510; doi: 10.34133/2022/9891510
- Nteroli G, Dasa MK, Messa G, et al. Two octaves spanning photoacoustic microscopy. Sci Rep 2022;12(1):10590; doi: 10.1038/s41598-022-14869-5
- 64. Hoffmann H. The glass frog tadpoles of Costa Rica (Anura: Centrolenidae): A study of morphology. Schweizerbart Science Publishers: Stuttgart, Germany; 2010; pp. 1–78.

65. Hoffmann H. Description of the previously unknown tadpole of *Hyalinobatrachium pulveratum* (Anura: Centrolenidae). Rev Biol Trop 2004; 52(1): 219–228; doi: 10.15517/rbt.v52i1.14912.

- Obika M, Bagnara JT. Pteridines as pigments in amphibians. Science 1964; 143(3605): 485–487; doi: 10.1126/science.143.3605.485.
- Bagnara JT, Taylor JD, Hadley ME. The dermal chromatophore unit. J Cell Biol 1968;38(1):67–79; doi: 10.1083/jcb.38.1.67
- Misuraca G, Prota G, Bagnara JT, et al. Identification of the leaf-frog melanophore pigment, rhodomelanochrome, as pterorhodin. Comp Biochem Physiol B Comp Biochem 1977;57:41–43; doi: 10.1016/0305-0491(77)90080-3
- Giovannetti R. The use of spectrophotometry UV-Vis for the study of porphyrins. Macro to Nano Spectroscopy 2012;87–108; doi: 10.5772/38797
- Prahl S. Optical absorption of hemoglobin. 1999. Available from: http://omlc. ogi.edu/spectra/hemoglobin [Last accessed: April 20, 2023].
- Choi TK, Choi TI, Lee YR, et al. Zebrafish as an animal model for biomedical research. Exp Mol Med 2021;53(3):310–317; doi: 10.1038/s12276-021-00571-5
- Mead AF, Kennedy GG, Palmer BM, et al. Mechanical characteristics of ultrafast zebrafish larval swimming muscles. Biophys J 2020;119(4):806–820; doi: 10.1016/j.bpj.2020.06.036
- 73. Hellfeld RV, Brotzmann K, Baumann L, et al. Adverse effects in the fish embryo acute toxicity (FET) test: A catalogue of unspecific morphological changes versus more specific effects in zebrafish (*Danio rerio*) embryos. Environ Sci Eur 2020;32:122; doi: 10.1186/s12302-020-00398-3
- Moore MJ, El-Rass S, Xiao Y, et al. Simultaneous ultra-high frequency photoacoustic microscopy and photoacoustic radiometry of zebrafish larvae in vivo. Photoacoustics 2018;12:14–21; doi: 10.1016/j.pacs.2018.08.004
- 75. Parichy DM, Elizondo MR, Mills MG, et al. Normal table of postembryonic zebrafish development: Staging by externally visible anatomy of the living fish. Dev Dynam 2009;238(12):2975–3015; doi: 10.1002/dvdy.22113
- Aman AJ, Fulbright AN, Parichy DM. Wnt/β-catenin regulates an ancient signaling network during zebrafish scale development. eLife 2018;7:e37001; doi: 10.7554/eLife.37001
- Rasmussen JP, Vo NT, Sagasti A. Fish scales dictate the pattern of adult skin innervation and vascularization. Dev Cell 2018;46(3):344–359.e4; doi: 10 .1016/j.devcel.2018.06.019
- 78. Behari J, Guha SK, Agarwal PN, Absorption spectra of bone. Calcif Tissue Res 1977:23(2):113–114: doi: 10.1007/BF02012774
- Johnson GA, Badea A, Brandenburg J, et al. An image-based reference for coordinating mouse brain research. Neuroimage 2010;53(2):365–372; doi: 10.1016/j.neuroimage.2010. 06.067
- Johansson JD, Spectroscopic method for determination of the absorption coefficient in brain tissue. J Biomed Opt 2010;15(5): 057005; doi: 10.1117/1. 2405710
- 81. Virani SS, Alonso A, Aparicio HJ, et al. Heart disease and stroke statistics-2021 update: A report from the American heart association. Circulation 2021;143:e254–e743; doi: 10.1161/CIR.000000000000950
- Žurauskas M, Barkalifa R, Alex A, et al. Assessing the severity of psoriasis through multivariate analysis of optical images from non-lesional skin. Sci Rep 2020;10(1):9154; doi: 10.1038/s41598-020-65689-4
- 83. Karlas A, Pleitez MA, Aguirre J, et al. Optoacoustic imaging in endocrinology and metabolism. Nat Rev Endocrinol 2021;17(6):323–335; doi: 10.1038/s41574-021-00482-5
- 84. Choi HS, Kim HK. Multispectral image-guided surgery in patients. Nat Biomed Eng 2020;4(3):245–246; doi: 10.1038/s41551-020-0536-7
- Labat-gest V, Tomasi S. Photothrombotic ischemia: A minimally invasive and reproducible photochemical cortical lesion model for mouse stroke studies.
   J Vis Exp 2013;(76):50370; doi: 10.3791/50370

Received: June 30, 2023 Accepted: September 19, 2023 Online Publication Date: October 16, 2023